Journal of Materials Chemistry A

PAPER

View Article Online
View Journal | View Issue

Cite this: *J. Mater. Chem. A*, 2018, **6**, 24783

Heterointerface engineering of trilayer-shelled ultrathin MoS_2/MoP/N-doped carbon hollow nanobubbles for efficient hydrogen evolution†

Jing-Qi Chi,‡[a] Yong-Ming Chai,‡[a] Xiao Shang,[a] Bin Dong,*[a] Chen-Guang Liu,[a] Wenjun Zhang[b] and Zhong Jin*[b]

Received 9th September 2018
Accepted 13th November 2018

DOI: 10.1039/c8ta08753a

rsc.li/materials-a

For efficient electrocatalysis, the rational construction of unique electrochemical interfaces is very important to enhance the intrinsic activity and expose more active sites. Herein, we demonstrate an atomic-migration-driven *in situ* thermal sulfurization–phosphorization strategy for the preparation of triple-layer-shelled hollow nanobubbles consisting of defect-rich ultrathin MoS_2/MoP outer layers and a porous N-doped carbon inner layer (MoS_2/MoP/NC) for efficient hydrogen evolution reaction (HER). In this method, $(NH_4)_2MoS_4$/NaH_2PO_4-blended polymer nanospheres were prepared *via* aqueous-phase reaction, followed by a one-step thermal annealing process. During the thermal treatment, the MoS_2 outer shell and NC inner layer were first formed at 500 °C; then the temperature was increased to 900 °C and the competitive reaction between the Mo atoms of the MoS_2 species formed a strong driving force to transfer P species from the interior to the surface of the porous NC layer and form an intermediate layer of MoP. This strategy realized the formation of ultrathin MoS_2/MoP/NC heterointerfaces with a high surface area (954.3 m^2 g^{-1}), abundant defect/edge sites, and improved electrocatalytic activity. In both acidic and alkaline solutions, the MoS_2/MoP/NC hollow nanobubbles exhibited low overpotentials (151 and 208 mV) to drive a current density of 10 mA cm^{-2}, small Tafel slopes (58 and 62 mV dec^{-1}), and excellent stability for hydrogen production, respectively. This work provides a new route for the construction of active electrochemical heterointerfaces for efficient electrocatalysis.

Introduction

The increasing global energy consumption together with the associated environmental issues has promoted the exploration of hydrogen power, which is viewed as a clean, renewable, and sustainable energy carrier.[1–4] Pollution-free hydrogen production from electrochemical water splitting has attracted enormous research interest.[5–7] However, the overpotential and performance decay of electrocatalysts must be minimized to fulfill the practical demands of the hydrogen evolution reaction (HER).[8–10] Although Pt-based catalysts are regarded as the most effective HER electrocatalysts, their high cost and scarcity hinder their scalable applications for the HER.[11–13] Therefore, the development of non-Pt electrocatalysts that can drive the HER with high efficiency at a lower overpotential is highly desirable for large-scale hydrogen production.[14,15]

Transition metal compounds, such as dichalcogenides[16,17] and phosphides[18,19] have been demonstrated as promising alternatives to replace Pt. Molybdenum disulfide (MoS_2), a typical two-dimensional nanomaterial, has been intensively investigated for the HER.[20–22] Among the possible crystalline phases of MoS_2, the 2H hexagonal phase is the most stable, but its layered nanostructures and semi-conductive property usually result in the stack/aggregation of active sites and poor conductivity.[16,17,23] Therefore, several strategies have been adopted to alleviate these shortcomings, such as preparing highly-dispersed MoS_2 nanostructures on conductive carbon materials to expose rich active sites and introducing heteroatoms to obtain a low hydrogen adsorption free energy (ΔG_{H^*}).[24,25] Another HER catalyst, molybdenum phosphide (MoP), exhibits superior intrinsic HER activity with a lower onset overpotential compared with MoS_2.[26,27] Moreover, the HER performance and stability of MoP can be further improved by introducing S heteroatoms.[28] However, the existing approaches to synthesize MoS_2/MoP hybrids are complicated, which usually consist of a number of different reagents and reactions, hindering their wide application.[29,30] On the other

[a]State Key Laboratory of Heavy Oil Processing, College of Science, China University of Petroleum (East China), Qingdao 266580, PR China. E-mail: dongbin@upc.edu.cn

[b]Key Laboratory of Mesoscopic Chemistry of MOE, School of Chemistry and Chemical Engineering, Nanjing University, Nanjing 210023, China. E-mail: zhongjin@nju.edu.cn

† Electronic supplementary information (ESI) available. See DOI: 10.1039/c8ta08753a

‡ These authors contributed equally to this work.

hand, the construction of highly-active electrochemical heterointerfaces with rich active sites and improving electronic conductivity are critical factors to improve catalytic activity.[31,32] Recently, N-doped carbon (NC) materials derived from organic polymers have been regarded as an ideal support for the preparation of hybrid catalysts due to their porous structure, large surface area, and good conductivity.[33,34] However, current approaches for preparing NC-supported composite catalysts usually involve simple mixing or encapsulating the active material into thick NC layers, which may decrease the electronic conductivity or hinder the exposure of rich active sites for the HER.[35] Therefore, it is very desirable to rationally construct closely-integrated and highly-active electrochemical heterointerfaces of MoS_2/MoP and NC to enhance the HER performance.

For the first time, herein, we report an *in situ* sulfurization–phosphorization strategy driven by thermal atomic-migration for the preparation of well-defined triple-layer-shelled hollow nanobubbles with ultrathin and compact few-layer MoS_2/MoP/NC heterointerfaces for efficient HER. Distinctive from previous studies, this strategy depends on the *in situ* and confined sulfurization and subsequent phosphorization reactions of the precursor $(NH_4)_2MoS_4/NaH_2PO_4$-blended polymer nanospheres at different temperatures. Initially, the few-layer epitaxial MoS_2 outer shell and NC inner layer were grown at 500 °C, and then the temperature was increased to 900 °C for generating a strong driving force to promote the atomic-migration of P species from the interior to the surface of the porous NC layer, forming an intermediate MoP layer. Benefiting from the synergistic effect, large surface area, and rich active sites of the MoS_2/MoP/NC heterointerfaces, the as-prepared trilayer-shelled hollow nanobubbles exhibited remarkable HER performances in both acidic and alkaline solutions, showing low overpotentials, low Tafel slopes, and excellent stability.

Experimental

Synthesis of $(NH_4)_2MoS_4/NaH_2PO_4$-blended polymer nanospheres as a precursor

Typically, 0.40 g of aniline, 0.30 g of pyrrole, 0.10 g of Triton X-100 surfactant, and 60 mL distilled water were homogenously mixed in a 100 mL beaker with rapid stirring for 0.5 h and strong ultrasonication for another 0.5 h. Subsequently, 20 mL aqueous solution of 1.90 g of $(NH_4)_2S_2O_8$ precooled at 0 °C was added to the above solution and maintained at 0 °C for 12 h to obtain uniform polymer nanospheres. After the polymerization reaction, the nanospheres were washed with distilled water six times, and then redispersed in 10 mL aqueous solution of 0.5 g $(NH_4)_2MoS_4$ and 1.0 g $NaH_2PO_4\cdot 2H_2O$ with strong ultrasonication for 1 h. Finally, the as-obtained mixture was vacuum-dried at 80 °C to form $(NH_4)_2MoS_4/NaH_2PO_4$-blended polymer nanospheres.

Synthesis of trilayer-shelled MoS_2/MoP/NC hollow nanobubbles

0.2 g of the above-prepared $(NH_4)_2MoS_4/NaH_2PO_4$-blended polymer nanospheres was thermally treated in a tube furnace at 500 °C and then 900 °C for 2 h at a heating rate of 5 °C min^{-1} in a flow of high-purity Ar. Then the tube furnace was cooled to room temperature naturally. The product was washed with distilled water and ethanol three times and vacuum-dried at 80 °C. To deeply understand the internal relationship between the nanostructures and activities of the MoS_2/MoP/NC heterolayers, several control samples were obtained under identical conditions except that the high pyrolyzation temperature was set to 800 °C or 1000 °C instead of 900 °C.

Synthesis of NC, MoS_2/NC, and MoP/NC nanobubbles as control samples

For comparison, pristine NC nanobubbles were prepared similarly to the MoS_2/MoP/NC nanobubbles but without the addition of $NaH_2PO_4\cdot 2H_2O$ and $(NH_4)_2MoS_4$. The MoS_2/NC control sample was prepared in the same way as the MoS_2/MoP/NC nanobubbles but without the addition of $NaH_2PO_4\cdot 2H_2O$. The MoP/NC control sample was synthesized in the same way as MoS_2/MoP/NC but with the addition of $(NH_4)_6Mo_7O_{24}\cdot 4H_2O$ instead of $(NH_4)_2MoS_4$.

Characterization

The morphologies and nanostructures of the samples were examined *via* SEM (Hitachi S-4800) and TEM (FEI Tecnai G^2, 200 kV). The elemental mappings and chemical compositions of the samples were characterized *via* energy-dispersive X-ray spectroscopy (EDX) equipped with a Hitachi S-4800. Crystallographic information and interlayer spacings were collected *via* X-ray diffraction (XRD, X'Pert PRO MPD diffractometer) with Cu Kα radiation (λ = 1.54 Å). Raman spectra were collected using a Renishaw inVia 2000 Raman spectrometer and 514 nm laser excitation. The BET surface areas and pore size distributions were collected using a Tristar II Plus system at liquid-nitrogen temperature. X-ray photoelectron spectroscopy (XPS) was performed on a Thermo Fisher Scientific II spectrometer to investigate the valence states of the obtained samples using an Al Kα source (1486.6 eV).

Electrochemical measurements

Electrochemical measurements were performed with a typical three-electrode setup using an electrochemical station (Gamry Reference 600) in 0.5 M H_2SO_4 or 1.0 M KOH. A certain amount of sample was loaded on a bare glassy carbon electrode (GCE) as the working electrode. Typically, 5 mg of sample powder was dispersed in 1 mL of co-solvent (v_{water}:$v_{ethanol}$ = 1 : 1) mixed with 20 μL of Nafion solution (5 wt%) under ultrasonication for 1 h. Then 5 μL of the resulting ink was pipetted onto the GCE and dried in air naturally. A saturated calomel electrode (SCE, Hg/Hg_2Cl_2 in saturated KCl) and a graphite rod were employed as the reference electrode and counter electrode, respectively. All potentials were calibrated with respect to the reversible hydrogen electrode (RHE): E(RHE) = E(SCE) + 0.243 + 0.059pH. Linear sweep voltammetry (LSV) measurements for the HER were conducted in 0.5 M H_2SO_4 (pH = 0) and 1.0 M KOH (pH = 14) at a scan rate of 5 mV s^{-1}. Electric impedance spectroscopy (EIS) was performed at a potential of −0.15 V (*vs.* RHE) in the

frequency range of 10^5 to 0.1 Hz under an amplitude of 5 mV. To evaluate the double-layer capacitances (C_{dl}), cyclic voltammograms (CV) were cycled in the non-faradaic region with sweep rates of 40, 60, 80, 100, and 120 mV s^{-1}, respectively. Long-term electrocatalytic stability tests were carried out *via* successive CV scans from −0.3 to 0.2 V (*vs.* RHE) at a sweep rate of 100 mV s^{-1} for 1000 cycles and chronoamperometric measurements at −0.2 V (*vs.* RHE) for 10 h.

Results and discussion

Preparation of MoS_2/MoP/NC hollow nanobubbles

The synthetic strategy for the MoS_2/MoP/NC hollow nanobubbles is exhibited in Fig. 1a. For the preparation of the MoS_2/MoP/NC hollow nanobubbles, $(NH_4)_2MoS_4$ was chosen as the Mo and S sources and $NaH_2PO_4 \cdot 2H_2O$ as the P source. The $(NH_4)_2MoS_4$ and $NaH_2PO_4 \cdot 2H_2O$ precursors with a mass ratio of 1 : 2 were mixed with polyaniline and pyrrole dissolved in water and then dried through evaporation to form $(NH_4)_2MoS_4$/NaH_2PO_4-blended polymer nanospheres. These precursor nanospheres provided confined nanospaces for the *in situ* sulfuration–phosphorization reactions during the following pyrolyzation treatment step, leading to the formation of MoS_2/MoP/NC hollow nanobubbles. At a relative low annealing temperature (500 °C) in an Ar atmosphere, the NC inner layer was formed through the carbonization of polyaniline and polypyrrole. $(NH_4)_2MoS_4$ was firstly reduced to MoS_3 and then partially converted to MoS_2 with gradually improved crystallinity tightly coupled on the surface of the carbon layer to form an MoS_2 outer shell, as shown by eqn (1) and (2):

$$(NH_4)_2MoS_4 \rightarrow MoS_3 + NH_3 + H_2S \quad (1)$$

$$MoS_3 \rightarrow MoS_2 + S \quad (2)$$

As the temperature increased to 900 °C, NaH_2PO_4 competitively reacted with the Mo species in MoS_2 on the surface of the carbon layer, promoting the transfer of P atoms from the interior to the surface of the porous NC layer and forming an intermediate layer of MoP layers. Accordingly, this atomic-migration-driven *in situ* thermal sulfurization–phosphorization strategy was used to prepare triple-layer-shelled hollow nanobubbles consisting of defect-rich ultrathin MoS_2/MoP outer layers and porous N-doped carbon inner layer.

Characterization of MoS_2/MoP/NC hollow nanobubbles

The morphologies and structural features of the pyrolyzed products were firstly characterized *via* SEM. As shown in Fig. S1a and S1b,† the pristine NC nanospheres display a well-defined spherical morphology with an average diameter of ~90 nm. The SEM images in Fig. S2–S4† and 1b reveal that the spherical shape of MoS_2/NC, MoP/NC, and MoS_2/MoP/NC nanobubbles was well-maintained, while their surface became rougher, indicating abundant active sites on their surface. The structural characteristics of the as-obtained MoS_2/MoP/NC nanobubbles were further examined *via* TEM, as depicted in Fig. S5† and 1c and d. The MoS_2/MoP/NC nanobubbles in Fig. S5† and 1c exhibit highly hollow interior voids, indicating bubble-like characteristics. A closer examination of the MoS_2/MoP/NC nanobubbles in Fig. 1d reveals that the ultrathin shells of the nanobubbles with a thickness of ~10 nm comprised of MoS_2, MoP, and NC trilayers are tightly coupled. The HRTEM examination of the edge of an MoS_2/MoP/NC nanobubble gave more information on its composition. Fig. 1e clearly shows that ultrathin MoS_2 layers (less than 10 layers) with rich defects were tightly adhered to form the outer shell. This results in better wettability and provides rich active sites for electrocatalysis. The interlayer distance between the MoS_2 layers was estimated to be 0.68 nm, which matches well with that of MoS_2 lattice structures. Moreover, the intermediate layer with an interplanar spacing of 0.28 nm adjacent to the MoS_2 layers corresponds to the (100) planes of the MoP layers. Especially, the close interaction of the MoS_2, MoP, and NC trilayers in the MoS_2/MoP/NC nanobubbles effectively will promote the electron transfer during electrocatalytic processes. To further explore the mechanism for the formation of the triple-layer-shelled MoS_2/MoP/NC hollow nanobubbles, the TEM images of NC, MoS_2, and MoP nanobubbles are also displayed for comparison. The TEM images of the pristine NC nanobubbles (Fig. S6a and S6b†) show a clear hollow core with a diameter of ~30 nm, implying that the thickness of the shell is ~30 nm. The formation of spherical NC nanostructures is derived from the confined interfacial polymerization of aniline and pyrrole in the presence of surfactants.[36] After introducing $(NH_4)_2MoS_4$ into the polymer, the MoS_2/NC nanobubbles were obtained, which were comprised of less than ten atomic layers tightly anchored on the NC surface to form the outer shell (Fig. S7a–S7c†). While for the MoP/NC nanobubbles, the MoP layer was formed with a decrease in the degree of hollowness compared with the MoS_2/NC nanobubbles (Fig. S8a and S8b†). The HRTEM (Fig. S8c†) image of the MoP/NC nanobubbles demonstrates the layered structure of the MoP layer with an interlayer distance of 0.28 nm, corresponding to the (100) planes of MoP. Comparison of the nanostructures of NC, MoS_2/NC, MoP/NC, and MoS_2/MoP/NC nanobubbles reveals that the MoS_2 layer was firstly formed on the surface of NC because $(NH_4)_2MoS_4$ is easily converted into MoS_2 at a relatively low temperature, as confirmed in Fig. S9,† where the MoS_2 layer is formed at a temperature as low as 500 °C. When the temperature increased to 900 °C, NaH_2PO_4 is prone to react with the Mo source derived from MoS_2, thus forming a strong driving force to transfer P species from the interior to the surface of the porous NC layer and then form an intermediate MoP layer. Therefore, it can be concluded that the ultrathin MoS_2/MoP/NC hollow nanobubbles comprised of triple-layer-shelled heterointerfaces were obtained through an atomic-migration-driven *in situ* thermal sulfurization–phosphorization process. The initial epitaxial growth of the MoS_2 layer is essential to the formation of ultrathin MoS_2/MoP/NC heterointerfaces, while providing a large exposed surface area, and the formation of the MoP layer can further improve the hollow degree of the MoS_2/MoP/NC nanobubbles. Moreover, the uniform distribution of elements on MoS_2/NC, MoP/NC, and MoS_2/MoP/NC nanobubbles is

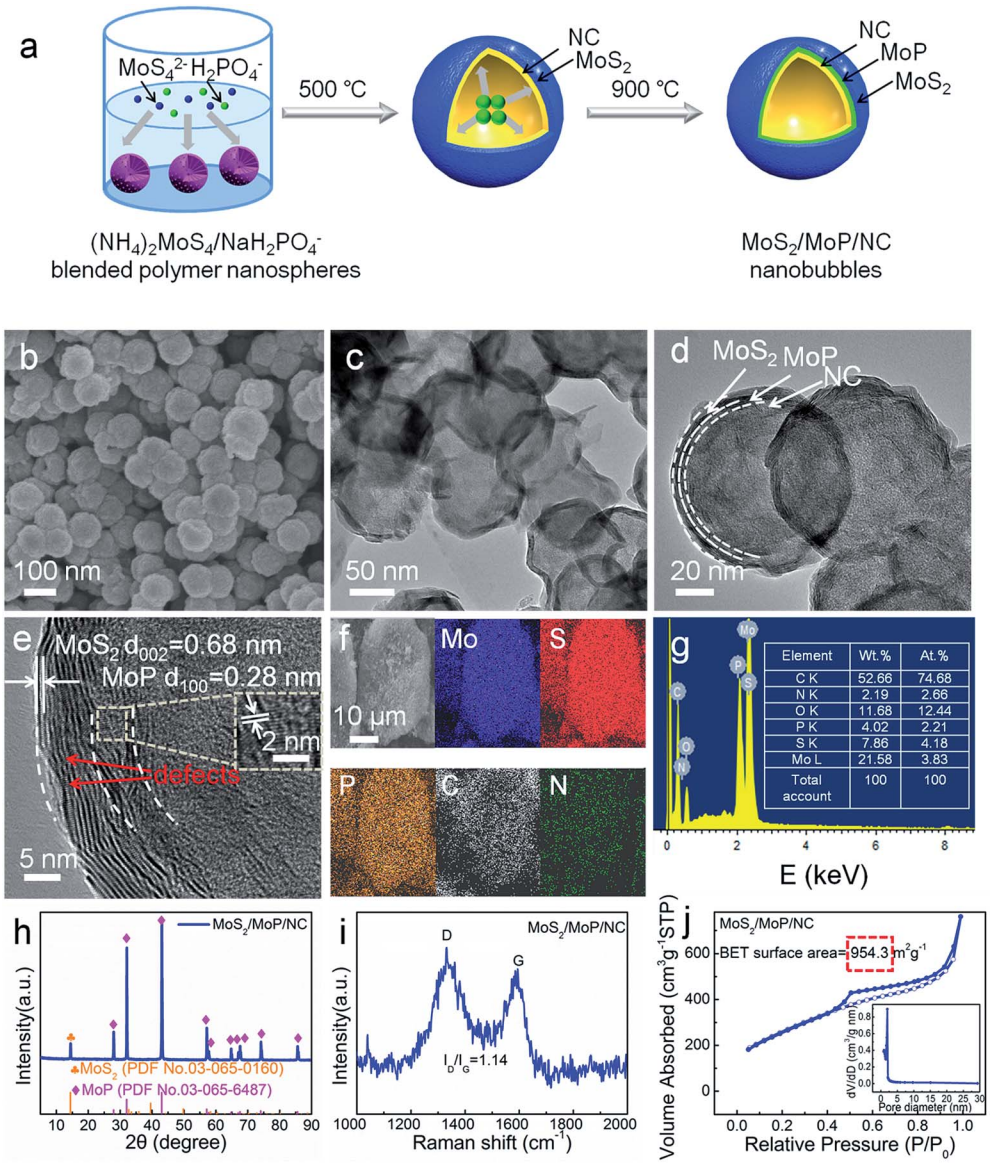

Fig. 1 (a) Schematic of the synthesis of the MoS_2/MoP/NC nanobubbles. (b) SEM image, (c and d) TEM images, (e) HRTEM image, (f) EDX mappings, (g) EDX elemental contents, (h) XRD pattern, (i) Raman spectrum, and (j) N_2 adsorption–desorption isotherm and pore size distribution of MoS_2/MoP/NC nanobubbles.

illustrated by the elemental mappings in Fig. S10† and 1f. The EDX spectrum in Fig. 1g also demonstrates that the MoS_2/MoP/NC nanobubbles are composed of Mo, S, P, C, N, and O elements. The Mo, S, and P elements account for the atomic percentages of 3.83%, 4.18%, and 2.21%, respectively. The EDX characterization of the MoS_2/NC and MoP/NC nanobubbles (Fig. S11a and S11b†) was also conducted to show the composition of the samples.

Fig. 1h shows the XRD patterns of the MoS_2/MoP/NC hollow nanobubbles. The XRD peaks can be ascribed to a mixture of MoS_2 (PDF no. 03-065-0160) and MoP (PDF no. 03-065-6487). A shark peak located at 14.4° is clearly observed, which is indexed to the (002) facets of MoS_2 and corresponds to the stacked MoS_2 layers in the *c*-direction. Moreover, the typical peaks for the hexagonal MoS_2 phase in the enlarged XRD patterns are clearly detected (Fig. S12†). The typical characteristic peaks located at 27.9°, 32.1°, 43.1°, 57.4°, 57.9°, 64.9°, 67.1°, 67.7°, and 85.6° are attributed to the (001), (100), (101), (110), (002), (111), (200), (102), and (112) facets of MoP, respectively. For comparison, the XRD patterns of the MoS_2/NC and MoP/NC nanobubbles are also displayed in Fig. S13.† For the NC nanospheres, the typical peak observed at 23° can be ascribed to the (002) facets of graphitic carbon. Moreover, the graphitization degree of the MoS_2/MoP/NC nanobubbles was further characterized *via* Raman spectroscopy (Fig. 1i). The two peaks at 1344 and 1590 cm^{-1} are indexed to the D and G bands of graphitic carbon, respectively. The I_D/I_G value was calculated to be 1.14, implying partial graphitization, which can effectively promote electron transfer in the MoS_2/MoP/NC nanobubbles.[37] The Brunauer–Emmett–Teller (BET) surface area of the MoS_2/MoP/

NC nanobubbles was calculated utilizing the nitrogen absorption technique. Fig. 1j shows that the MoS_2/MoP/NC nanobubbles exhibit a typical mesoporous structure, as evidenced by their high specific BET surface area of up to 954.3 $m^2\ g^{-1}$ and numerous nanopores centered at 2.4 nm (the inset of Fig. 1j). To reveal the effect of the initially-formed MoS_2 layer and MoP layer on the MoS_2/MoP/NC nanobubbles, the BET surface areas of the MoP/NC and MoS_2/NC control samples were also measured (Fig. S14 and S15,† respectively). As shown in Fig. S14,† the MoP/NC nanobubbles exhibit a much smaller BET surface area of 122.4 $m^2\ g^{-1}$ with the size of their nanopores centered at 2.5 nm. The MoS_2/NC nanobubbles exhibit a BET surface area of 390.8 $m^2\ g^{-1}$ with an average pore size of 3.5 nm (Fig. S15†). This indicates that the MoS_2 and MoP layers are both responsible for the large surface area of the MoS_2/MoP/NC nanobubbles. The unique porous structure of the MoS_2/MoP/NC nanobubbles with high uniformity would expose rich active sites for electrocatalysis and facilitate the mass transfer of the electrolyte (Table S1†).

The chemical compositions and valence states of the MoS_2/MoP/NC nanobubbles were further characterized *via* XPS. The XPS survey spectrum exhibits the obvious signals Mo, S, P, C, N, and O (Fig. 2a). As shown in Fig. 2b, the high-resolution XPS spectrum in the Mo 3d region can be deconvoluted into two separate doublets. The Mo 3d peaks at 228.2 and 231.2 eV represent the characteristic doublet of Mo^{4+} arising from the MoS_2 species,[38,39] which shifted by ~0.8 eV compared with that for 2H-MoS_2 (229 eV). The doublet peaks at 228.7 and 232.1 eV can be indexed to $Mo^{\delta+}$ ($0 \leq \delta \leq 4$) species, confirming the presence of MoP.[40,41] In the S 2p region (Fig. 2c), the peaks at 161.9 and 163.1 eV correspond to the S^{2-} $2p_{3/2}$ and S^{2-} $2p_{1/2}$ species, respectively.[42,43] In addition, the peaks at 163.9 and 165.1 eV with an energy level difference of ~1.2 eV can be indexed to S_2^{2-} $2p_{3/2}$ and S_2^{2-} $2p_{1/2}$, respectively.[44] The doublet peaks at 129.4 and 130.2 eV in the P 2p region (Fig. 2d) are typical peaks of MoP.[45] The other broad peak at 133 eV is attributed to PO_4^{3-} or P_2O_5 species formed by slight surface oxidation.[46] The N 1s spectrum (Fig. 2e) can be divided into three peaks at 398.7, 400.5, and 401.6 eV, indexed to pyridinic-N, pyrrolic-N, and quaternary-N, respectively, which imply the successful doping of N into the carbon matrix.[47,48] The C 1s spectrum in Fig. 2f can be divided into four signals at 284.2, 284.6, 285, and 285.7 eV, which are ascribed to C–C/C=C, C–O, C=O, and C–N, respectively.[49,50] The introduction of electron-rich dopants (such as N heteroatoms) into the carbon matrix can tune its electronic configuration efficiently, thus boosting its intrinsic activity for the HER.[26] The existence of C–O and C=O bonds is inevitable when the C-doped catalysts are prepared at high temperature in an inert atmosphere due to the combination of C with O species and their oxidation. Moreover, according to the XPS results, Mo, S, P and C elements account for the weight percentages of 22.08%, 7.85%, 4.51% and 53.15%, respectively. The ICP measurements further demonstrated that the Mo, S, P and C elements account for the weight percentages of 22.15%, 7.83%, 4.48% and 53.02%, respectively, which is in accordance with the XPS results. According the different area ratios in the Mo 3d, S 2p, P 2p, and C 1s regions, the loading amount of MoS_2, MoP and NC was calculated to be 8.82%, 22.21%, and 53%, respectively. For comparison, the XPS survey spectra of the MoS_2/NC and MoP/NC control samples are also displayed in Fig. S16a.† The Mo^{4+} 3d peak of the MoS_2/MoP/NC nanobubbles shifted to a lower binding energy compared to that of the MoS_2/NC nanobubbles and the $Mo^{\delta+}$ 3d peak of the MoS_2/MoP/NC nanobubbles shifted to higher binding energy compared to that of MoP/NC nanobubbles, demonstrating the electronic interaction between MoS_2 and

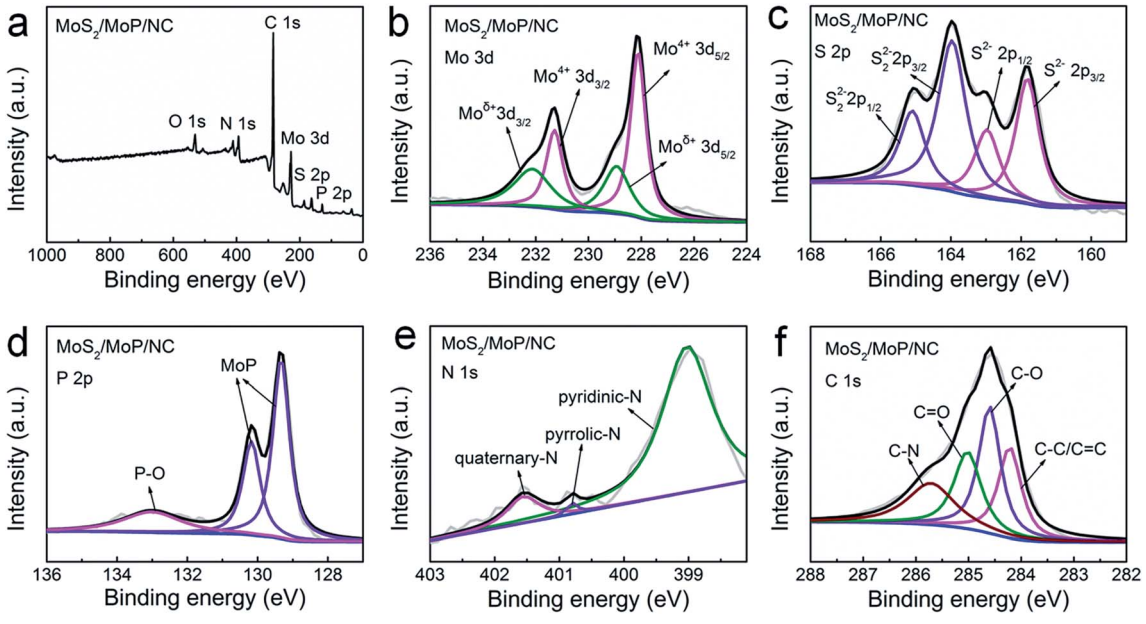

Fig. 2 (a) Survey XPS spectrum and (b–f) high-resolution XPS scans of MoS_2/MoP/NC nanobubbles in the (b) Mo 3d, (c) S 2p, (d) P 2p, (e) N 1s, and (f) C 1s regions.

MoP in the MoS_2/MoP/NC nanobubbles. The binding energy of the S^{2-} 2p peak of the MoS_2/MoP/NC nanobubbles is lower than that of the MoS_2/NC nanobubbles (Fig. S16b†), which is due to the higher electronegativity of S than P. Electrons tend to transfer from P to S, leading to the lower binding energy of S in MoS_2/MoP/NC nanobubbles. This electron transfer effect is also reflected in the binding energy shifts of the P 2p peak of the MoS_2/MoP/NC nanobubbles (Fig. S16c†), which shifted to a higher value compared with that for the MoP/NC nanobubbles. These results indicate the existence of an electronic interaction effect in the MoS_2/MoP/NC nanobubbles, which contributes to their enhanced electrocatalytic performance due to the electronic interaction between P and S, leading to a decrease in ΔG_{H^*}.[51]

To investigate the relationship between the structure and activity of the MoS_2/MoP/NC heterolayers, a series of control samples were also synthesized by varying the pyrolyzation temperature, which were analyzed *via* SEM, (HR)TEM, EDX, XRD, and Raman spectroscopy (Fig. 3, S17 and S18†). Fig. 3a–f show that the as-obtained MoS_2/MoP/NC nanobubbles had a decreased diameter when the temperature increased from 800 °C to 1000 °C. Moreover, the microstructure of the MoS_2/MoP/NC nanobubbles was maintained well at 1000 °C, indicating their high thermal stability. The EDX mappings in Fig. S17a and S17b† show that the Mo, S, P, C, and N elements in the control samples are homogenously distributed. EDX measurements were further conducted to present the elemental contents of the control samples (Fig. S18a and S18b†). As is known, the N heteroatoms introduced in the NC layers could enhance the electrocatalytic performance of the catalyst by tuning its electronic structure. Fig. S18a and S18b† show that the contents of N element declined with an increase in the pyrolyzation temperature, which may result in an inferior HER performance. Moreover, the XRD patterns in Fig. 3g show that the contents of MoS_2 and MoP also changed with the temperature. The MoP layer became more evident as the temperature

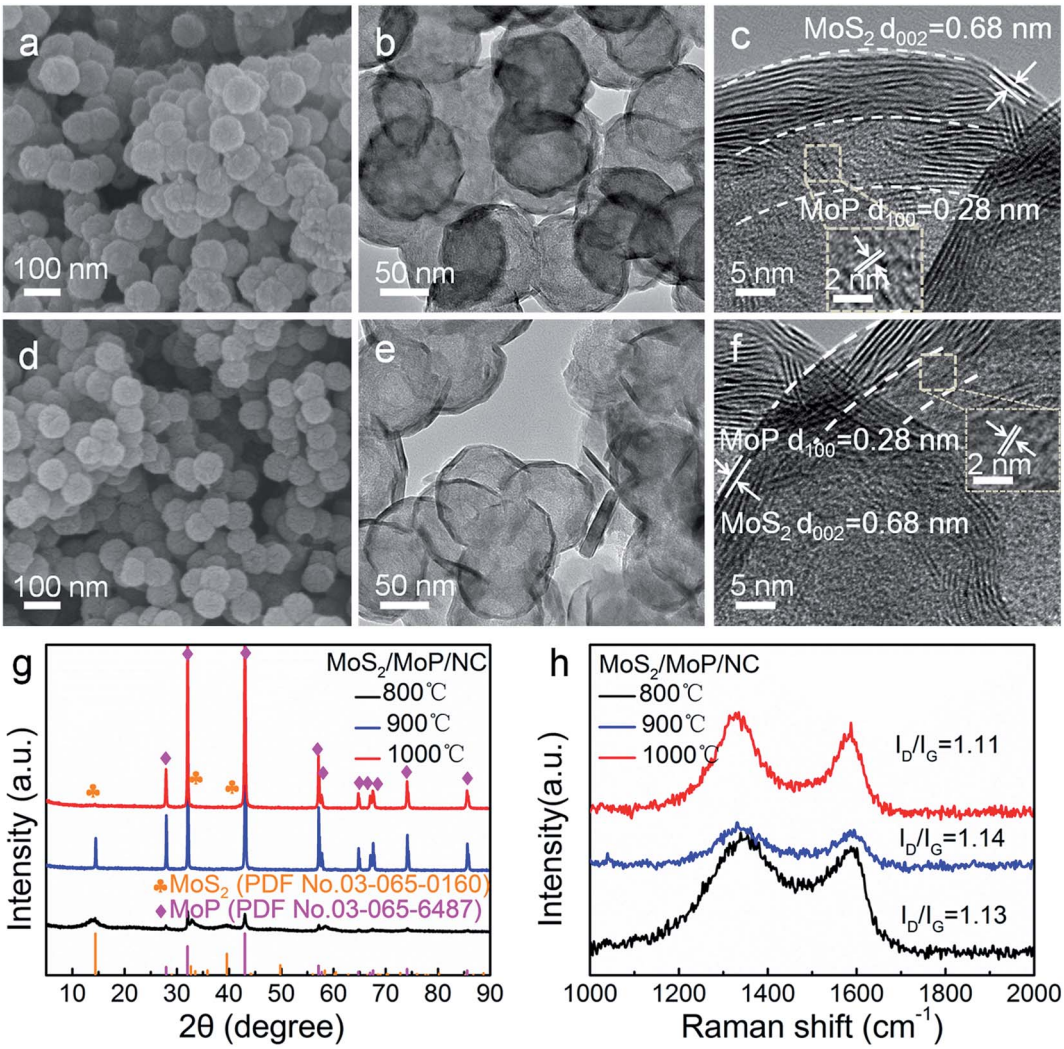

Fig. 3 (a) SEM, (b) TEM, and (c) HRTEM images of the MoS_2/MoP/NC control sample prepared at 800 °C. (d) SEM, (e) TEM, and (f) HRTEM images of the MoS_2/MoP/NC control sample prepared at 1000 °C. (g) XRD patterns and (h) Raman spectra of the MoS_2/MoP/NC nanobubbles obtained at 800 °C, 900 °C, and 1000 °C.

increased from 800 °C to 1000 °C, implying that MoP is likely to be formed at a high temperature. The Raman results in Fig. 3h indicate that the I_D/I_G values of the MoS_2/MoP/NC control samples have almost no change, demonstrating the similar graphitization level of the NC layers in all the samples.

HER performances of MoS_2/MoP/NC hollow nanobubbles

The electrocatalytic HER activity of the MoS_2/MoP/NC electrode was firstly tested in an N_2-saturated acidic solution. Similarly, the HER activities of the bare GCE, NC, MoS_2/NC and MoP/NC electrodes were also investigated for comparison. In the polarization curves (Fig. 4a), the bare GCE electrode showed very poor HER activity, which excludes the effect of the bare GCE on the catalytic performance. Impressively, the MoS_2/MoP/NC electrode presented a dramatically enhanced performance with an overpotential (η) of only 151 mV at a current density of 10 mA cm^{-2}, which is lower than that of the NC (660 mV), MoS_2/NC (281 mV), and MoP/NC (160 mV) electrodes. The overpotential of the MoS_2/MoP/NC electrode was 130 mV lower than that of the MoS_2/NC electrode, indicating that the incorporation of P species in the triple-layer-shelled hollow nanobubbles plays a key role in promoting the electrochemical activity. The synergistic effect between the P and S species could cause a significant decrease in ΔG_{H^*} for neighboring S atoms, indicating the existence of surface active MoS_2 species.[51]

The Tafel slope can be determined from the LSV curve *via* the Tafel equation ($\eta = a + b \log j$, where a is a constant and b is the Tafel slope) to evaluate the HER mechanism (Fig. 4b). Typically, the HER process has two steps in acidic conditions, where the first step is the Volmer (eqn (3)) reaction and the second is the Heyrovsky (eqn (4)) or Tafel reaction (eqn (5)):[52]

$$H_3O^+ + e^- \rightarrow H_{ads} + H_2O \quad (3)$$

$$H_{ads} + H_3O + e^- \rightarrow H_2 + H_2O \quad (4)$$

$$H_{ads} + H_{ads} \rightarrow H_2 \quad (5)$$

The Tafel slope of the MoS_2/MoP/NC electrode was as low as 58 mV dec^{-1}, indicating that the release of H_2 is the rate-determining step and the HER process on the MoS_2/MoP/NC electrode follows the Volmer–Heyrovsky mechanism. The Tafel slope of the MoS_2/MoP/NC electrode was significantly lower than that of NC (126 mV dec^{-1}), MoS_2/NC (112 mV dec^{-1}), and MoP/NC (66 mV dec^{-1}), demonstrating the favorable HER kinetics of the MoS_2/MoP/NC electrode.

The double layer capacitance (C_{dl}) at the solid–liquid interface was further calculated using the cyclic voltammetry (CV) method to assess the linearly-related electrochemical surface area (ECSA). The typical CV results of the MoS_2/MoP/NC electrode at varying scan rates from 40 to 120 mV s^{-1} are exhibited in Fig. 4c. The measured C_{dl} values of the NC, MoS_2/NC, MoP/NC, and MoS_2/MoP/NC electrodes were calculated to be 1.3, 5.3, 3.3, and 15.1 mF cm^{-2}, respectively (Fig. 4d). The large C_{dl} value of the MoS_2/MoP/NC electrode indicates a large ECSA with

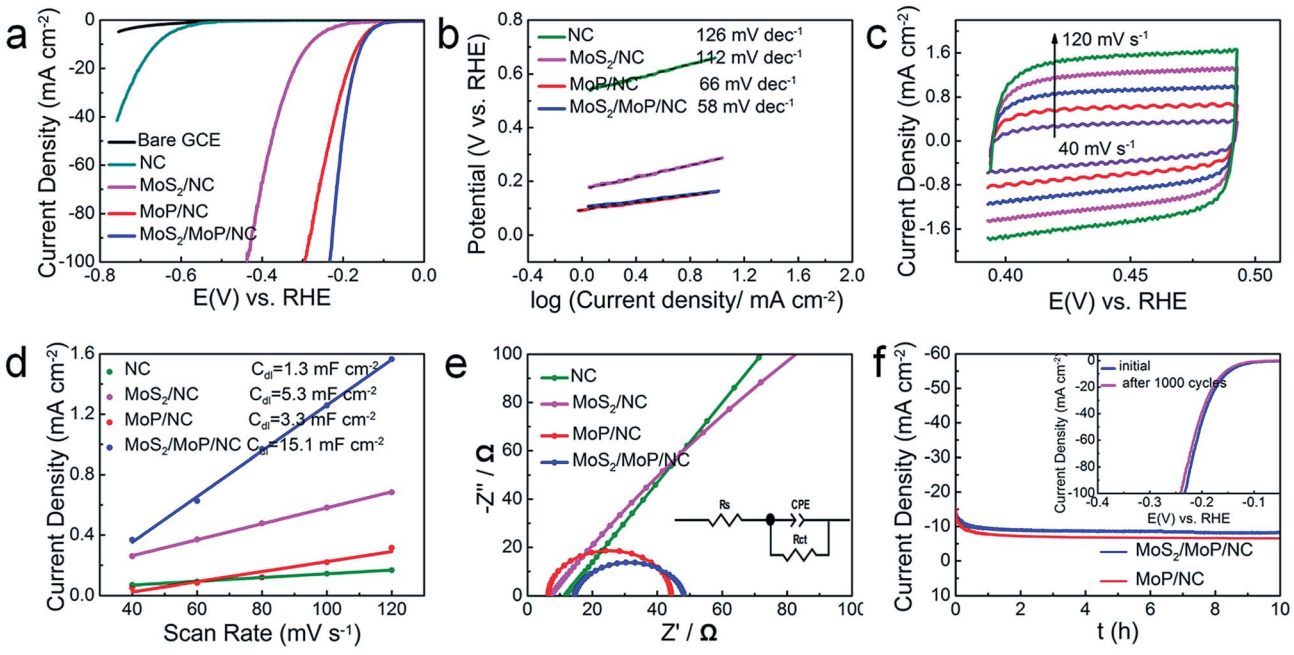

Fig. 4 (a) Polarization curves of the bare GCE, NC, MoS_2/NC, MoP/NC, and MoS_2/MoP/NC electrodes at a scan rate of 5 mV s^{-1}. (b) Tafel plots calculated from (a). (c) Cyclic voltammograms (CV) from the double-layer capacitance measurement of the MoS_2/MoP/NC nanobubbles, which were collected in a selected potential range without faradic current at different scanning rates (40–120 mV s^{-1}). (d) Double-layer capacitances of NC, MoS_2/NC, MoP/NC, and MoS_2/MoP/NC nanobubbles. (e) Nyquist plots of NC, MoS_2/NC, MoP/NC, and MoS_2/MoP/NC nanobubbles at a potential of −0.15 V (*vs.* RHE). (f) Chronoamperometry curves of the MoP/NC and MoS_2/MoP/NC nanobubbles during the HER process over 10 h at a fixed overpotential of 200 mV. The inset of (f) shows the HER polarization curves of the MoS_2/MoP/NC nanobubbles before and after 1000 CV cycles from −0.3 to 0.2 V (*vs.* RHE) in 0.5 M H_2SO_4.

rich active sites towards the HER, which may arise from its large BET surface area (954.3 m^2 g^{-1}). EIS measurements were also performed on the samples to gain further insight into their electrode kinetics (Fig. 4e). By fitting the equivalent circuit inserted in Fig. 4e, the charge transfer resistances (R_{ct}) of all the samples are presented in Table S2.† The results show that the R_{ct} value of the MoS_2/MoP/NC electrode (31.36 Ω) is much smaller than that of NC (28 514 Ω), MoS_2/NC (921.3 Ω), and MoP/NC (33.9 Ω), indicating its faster charge transfer rate for the HER. The small resistance of the MoS_2/MoP/NC electrode may be related to its partial graphitization ($I_D/I_G = 1.14$), high conductivity of NC and MoP, and synergistic effect among the NC, MoS_2, and MoP layers, which can effectively promote the charge transfer between the MoS_2/MoP/NC electrode and electrolyte.

The electrocatalytic stability of catalysts is a vital factor for their practical applications. Therefore, the durability of the MoS_2/MoP/NC electrode was investigated *via* chronoamperometry for 10 h and also continuous CV for 1000 cycles at a scan rate of 100 mV s^{-1}. The chronoamperometric curve of the MoS_2/MoP/NC electrode (Fig. 4f) shows that its current density was only degraded slightly after operation for 10 h in acidic medium. Furthermore, as shown in the inset of Fig. 4f, the polarization curve of the MoS_2/MoP/NC electrode exhibited a slightly negative shift after 1000 sweeps, which is in accordance with the chronoamperometric measurement. The excellent stability of the MoS_2/MoP/NC electrode may be ascribed to the MoS_2/MoP layers tightly coupled with NC layers, which prevent the corrosion and agglomeration of the active species.

The electrocatalytic activity of the MoS_2/MoP/NC electrode for the HER in alkaline media was also evaluated. As expected, the MoS_2/MoP/NC electrode also exhibited an enhanced HER performance in 1.0 M KOH, showing a low overpotential of only 208 mV at 10 mA cm^{-2}, which is 112 mV lower than that of MoS_2/NC (Fig. S19a†). Moreover, the MoS_2/MoP/NC electrode showed a lower Tafel slope of 62 mV dec^{-1}, which is lower than that of NC (154 mV dec^{-1}), MoS_2/NC (113 mV dec^{-1}), and MoP/NC (70 mV dec^{-1}), suggesting a possible Volmer–Heyrovsky mechanism (Fig. S19b†). Furthermore, the MoS_2/MoP/NC electrode exhibited a large C_{dl} of 6.7 mF cm^{-2} (Fig. S19c and S19d†) and a small R_{ct} of 25.6 Ω (Fig. S19e and Table S2†). The stability tests *via* both chronoamperometry and successive CV analysis demonstrated that the electrocatalytic stability of MoS_2/MoP/NC is higher than that of MoP/NC in alkaline solution (Fig. S19f†). Overall, all the HER measurements prove that the MoS_2/MoP/NC electrode possesses superior activity and stability in both acidic and alkaline solutions.

To further interpret the relationship between the nanostructures and activities of the MoS_2/MoP/NC heterolayers, the HER performances of the MoS_2/MoP/NC control samples obtained at different pyrolyzation temperatures were also investigated in acidic and alkaline solutions. The overpotentials of the MoS_2/MoP/NC samples obtained at 800 °C, 900 °C, and 1000 °C in a solution of 0.5 M H_2SO_4 at 10 mA cm^{-2} were 208, 151, and 199 mV, and the corresponding Tafel slopes were 86, 58, and 85 mV dec^{-1}, respectively (Fig. 5a and b), indicating the superior HER performance of the MoS_2/MoP/NC sample obtained at 900 °C. Fig. 5c and d, and Table S3† show that the MoS_2/MoP/NC samples obtained at 800 °C and 1000 °C exhibit smaller C_{dl} and larger R_{ct} values than that obtained at 900 °C. The HER performances of the MoS_2/MoP/NC control samples in alkaline media are in accordance with the results tested in acidic solution (Fig. S20a–S20d†). The MoS_2/MoP/NC sample obtained at 900 °C exhibited the optimal HER activity, possibly because this

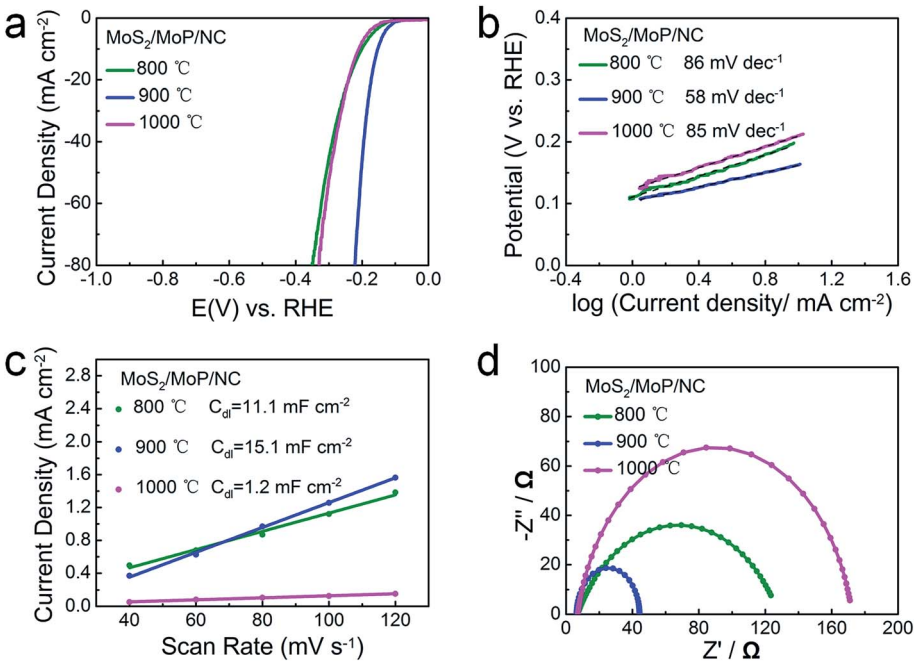

Fig. 5 (a) Polarization curves, (b) Tafel plots, (c) double-layer capacitance, and (d) Nyquist plots of the MoS_2/MoP/NC nanobubbles obtained at 800 °C, 900 °C, and 1000 °C measured in 0.5 M H_2SO_4 solution.

sample has integrated the superiority of well-dispersed active species, optimal atomic ratio of MoS_2/MoP species, optimal partial graphitization, and high N-doping content. Overall, the electrochemical measurements demonstrate that the pyrolyzation temperature is critical for the formation of highly active heterointerfaces.

The excellent HER performances of the MoS_2/MoP/NC nanobubbles may be ascribed to the following reasons: (1) the atomic-migration-driven *in situ* thermal sulfurization–phosphorization process leads to the formation of highly active electrochemical heterointerfaces, (2) the synergistic effect among the NC, MoS_2, and MoP layers enhances the electrochemical performances, (3) the N heteroatoms doped in the NC layer can tune the electronic configuration effectively, thus improving the intrinsic activity for the HER and (4) the high specific surface area (954.3 $m^2\ g^{-1}$) of the MoS_2/MoP/NC hollow nanobubbles is beneficial for exposing rich active sites and accelerating mass transfer between the electrode and electrolyte.

Conclusions

In summary, triple-layer-shelled hollow nanobubbles consisting of defect-rich ultrathin MoS_2/MoP outer layers and porous NC inner layer were realized through an atomic-migration-driven *in situ* thermal sulfurization–phosphorization strategy for enhanced HER performances. This strategy relies on *in situ* and confined sulfurization and subsequent phosphorization reactions of precursor $(NH_4)_2MoS_4/NaH_2PO_4$-blended polymer nanospheres at different temperatures. The P species migrate from the interior to the surface of the porous NC layer and competitively reacts with the Mo atoms in MoS_2, forming the intermediate layer of MoP. The MoS_2/MoP/NC hollow nanobubbles exhibit enhanced electrocatalytic activity and excellent stability for the HER in both acidic and alkaline solutions. Utilizing this novel strategy to construct active electrochemical heterointerfaces may open a new approach for the design of advanced electrocatalysts for various electrocatalytic processes.

Conflicts of interest

There are no conflicts to declare.

Acknowledgements

This work is fnancially supported by the National Natural Science Foundation of China (21776314, 21573108, 51761135104, 21872069), National Key R&D Program of China (2017YFA0208200, 2016YFB0700600, 2015CB659300), Shandong Provincial Natural Science Foundation (ZR2017MB059), Natural Science Foundation of Jiangsu Province (BK20180008), High-Level Entrepreneurial and Innovative Talents Program of Jiangsu Province, and the Fundamental Research Funds for the Central Universities (18CX05016A, 020514380146).

References

1 X. X. Zou and Y. Zhang, *Chem. Soc. Rev.*, 2015, **44**, 5148–5180.
2 W. J. Zhou, J. Jia, J. Lu, L. Yang, D. Hou, G. Li and S. Chen, *Nano Energy*, 2016, **28**, 29–43.
3 A. Ambrosi and M. Pumera, *ACS Catal.*, 2016, **6**, 3985–3993.
4 Q. Ding, B. Song, P. Xu and S. Jin, *Chem*, 2016, **1**, 699–726.
5 B. Dong, X. Zhao, G. Q. Han, X. Li, X. Shang, Y. R. Liu, W. H. Hu, Y. M. Chai, H. Zhao and C. G. Liu, *J. Mater. Chem. A*, 2016, **4**, 13499–13508.
6 G. Han, Y. H. Jin, R. A. Burgess, N. E. Dickenson, X. M. Cao and Y. Sun, *J. Am. Chem. Soc.*, 2017, **139**, 15584–15587.
7 Z. W. Seh, J. Kibsgaard, C. F. Dickens, I. Chorkendorff, J. K. Nørskov and T. F. Jaramillo, *Science*, 2017, **355**, 6321.
8 X. J. Chua, J. Luxa, A. Eng, S. M. Tan, Z. Sofer and M. Pumera, *ACS Catal.*, 2016, **6**, 5724–5734.
9 X. Chia, A. Y. S. Eng, A. Ambrosi, S. M. Tan and M. Pumera, *Chem. Rev.*, 2015, **115**, 11941–11966.
10 X. Shang, K. L. Yan, Y. Rao, B. Dong, J. Q. Chi, Y. R. Liu, X. Li, Y. M. Chai and C. G. Liu, *Nanoscale*, 2017, **9**, 12353–12363.
11 Y. Q. Zhang, B. Ouyang, J. Xu, G. Jia, S. Chen, R. S. Rawat and H. J. Fan, *Angew. Chem., Int. Ed.*, 2016, **55**, 8670–8674.
12 X. Zou, Y. Liu, G. Li, Y. Wu, D. Liu, W. Li, H. Li, D. Wang, Y. Zhang and X. Zou, *Adv. Mater.*, 2017, **29**, 1700404.
13 J. Chi, W. Gao, J. Lin, B. Dong, J. Qin, Z. Liu, B. Liu, Y. Chai and C. Liu, *J. Catal.*, 2018, **360**, 9–19.
14 C. C. L. McCrory, S. Jung, I. M. Ferrer, S. M. Chatman, J. C. Peters and T. F. Jaramillo, *J. Am. Chem. Soc.*, 2015, **137**, 4347–4357.
15 E. Parzinger, E. Mitterreiter, M. Stelzer, F. Kreupl, J. W. Ager, A. W. Holleitner and U. Wurstbauer, *Applied Materials Today*, 2017, **8**, 132–140.
16 X. Shang, W. H. Hu, X. Li, B. Dong, Y. R. Liu, G. Q. Han, Y. M. Chai and C. G. Liu, *Electrochim. Acta*, 2017, **224**, 25–31.
17 C. Tang, W. Wang, A. Sun, C. Qi, D. Zhang, Z. Wu and D. Wang, *ACS Catal.*, 2015, **5**, 6956–6963.
18 Z. Xing, Q. Liu, A. M. Asiri and X. Sun, *Adv. Mater.*, 2014, **26**, 5702–5707.
19 A. Han, H. Chen, H. Zhang, Z. Sun and P. Du, *J. Mater. Chem. A*, 2016, **4**, 10195–10202.
20 H. Yu, Y. Xue, L. Hui, C. Zhang, Y. Zhao, Z. Li and Y. Li, *Adv. Funct. Mater.*, 2018, **28**, 1707564.
21 X. Li, J. Zhang, R. Wang, H. Huang, C. Xie, Z. Li, J. Li and C. Niu, *Nano Lett.*, 2015, **15**, 5268–5272.
22 G. Li, D. Zhang, Q. Qiao, Y. Yu, D. Peterson, A. Zafar, R. Kumar, S. Curtarolo, F. Hunte, S. Shannon, Y. Zhu, W. Yang and L. Cao, *J. Am. Chem. Soc.*, 2016, **138**, 16632–16638.
23 R. Ye, A. Vicente, Y. Liu, J. A. Jimenez, Z. Peng, T. Wang, Y. Li, B. I. Yakobson, S. Wei and M. Yacaman, *Adv. Mater.*, 2015, **28**, 1427–1432.
24 K. Zhang, Y. Zhao, D. Fu and Y. Chen, *J. Mater. Chem. A*, 2015, **3**, 5783–5788.
25 J. S. Li, Y. Wang, C. H. Liu, S. L. Li, Y. G. Wang, L. Z. Dong, Z. H. Dai, Y. F. Li and Y. Q. Lan, *Nat. Commun.*, 2016, **7**, 11204.
26 X. Huang, M. Leng, W. Xiao, M. Li, J. Ding, T. L. Tan, W. S. V. Lee and J. Xue, *Adv. Funct. Mater.*, 2017, **27**, 1604943.
27 S. Carenco, D. Portehault, C. Boissière, N. Mèzailles and C. Sanchez, *Chem. Rev.*, 2013, **113**, 7981–8065.

28 J. Kibsgaard and T. F. Jaramillo, *Angew. Chem., Int. Ed.*, 2014, **53**, 14433–14437.
29 W. Zhu, C. Tang, D. Liu, J. Wang, A. M. Asiri and X. Sun, *J. Mater. Chem. A*, 2016, **4**, 7169–7173.
30 P. Liu, J. Zhu, J. Zhang, P. Xi, K. Tao, D. Gao and D. P. Xue, *ACS Energy Lett.*, 2017, **2**, 745–752.
31 W. Zhou, K. Zhou, D. Hou, X. Liu, G. Li, Y. Sang, H. Liu, L. Li and S. Chen, *ACS Appl. Mater. Interfaces*, 2014, **6**, 21534–21540.
32 Y. Yan, B. Xia, X. Ge, Z. Liu, J. Y. Wang and X. Wang, *ACS Appl. Mater. Interfaces*, 2013, **5**, 12794–12798.
33 Y. Huang, Q. Gong, X. Song, K. Feng, K. Nie, F. Zhao, Y. Wang, M. Zeng, J. Zhong and Y. Li, *ACS Nano*, 2016, **10**, 11337–11343.
34 J. Chi, W. Gao, J. Lin, B. Dong, K. Yan, J. Qin, B. Liu, Y. Chai and C. Liu, *ChemSusChem*, 2018, **11**, 743–752.
35 Y. Tang, C. Liu, W. Huang, X. Wang, L. Dong, S. Li and Y. Lan, *ACS Appl. Mater. Interfaces*, 2017, **9**, 16977–16985.
36 C. Q. Zhou, J. Han, G. P. Song and R. Guo, *J. Polym. Sci., Part A: Polym. Chem.*, 2008, **46**, 3563–3572.
37 F. J. Maldonado-Hodar, C. Moreno-Castilla, J. Rivera-Utrilla, Y. Hanzawa and Y. Yamada, *Langmuir*, 2000, **16**, 4367–4373.
38 Y. J. Tang, M. R. Gao, C. H. Liu, S. L. Li, H. L. Jiang, Y. Q. Lan, M. Han and S. H. Yu, *Angew. Chem., Int. Ed.*, 2015, **54**, 12928–12932.
39 H. Vrubel, D. Merki and X. L. Hu, *Energy Environ. Sci.*, 2012, **5**, 6136–6144.
40 J. Bai, X. Li, A. J. Wang, R. Prins and Y. Wang, *J. Catal.*, 2012, **287**, 161–169.
41 P. Xiao, M. A. Sk, L. Thia, X. M. Ge, R. J. Lim, J. Y. Wang, K. H. Lim and X. Wang, *Energy Environ. Sci.*, 2014, **7**, 2624–2629.
42 D. Merki, S. Fierro, H. Vrubel and X. L. Hu, *Chem. Sci.*, 2011, **2**, 1262–1267.
43 T. W. Lin, C. J. Liu and J. Y. Lin, *Appl. Catal., B*, 2013, **134–135**, 75–82.
44 C. G. Morales-Guio and X. L. Hu, *Acc. Chem. Res.*, 2014, **47**, 2671–2681.
45 L. Zhang, S. Li, H. Tan, S. U. Khan, Y. Ma, H. Zang, Y. Wang and Y. Li, *ACS Appl. Mater. Interfaces*, 2017, **9**, 16270–16279.
46 J. S. Li, Y. J. Tang, C. H. Liu, S. L. Li, R. H. Li, L. Z. Dong, Z. H. Dai, J. C. Bao and Y. Q. Lan, *J. Mater. Chem. A*, 2016, **4**, 1202–1207.
47 Y. Zheng, Y. Jiao, L. H. Li, T. Xing, Y. Chen, M. Jaroniec and S. Z. Qiao, *ACS Nano*, 2014, **8**, 5290–5296.
48 S. P. Wang, J. Wang, M. L. Zhu, X. B. Bao, B. Y. Xiao, D. F. Su, H. R. Li and Y. Wang, *J. Am. Chem. Soc.*, 2015, **137**, 15753–15759.
49 H. J. Yan, C. G. Tian, L. Wang, A. P. Wu, M. C. Meng, L. Zhao and H. G. Fu, *Angew. Chem., Int. Ed.*, 2015, **54**, 6325–6329.
50 W. Ai, Z. M. Luo, J. Jiang, J. H. Zhu, Z. Z. Du, Z. X. Fan, L. H. Xie, H. Zhang, W. Huang and T. Yu, *Adv. Mater.*, 2014, **26**, 6186–6192.
51 Z. Shi, K. Nie, Z. Shao, B. Gao, H. Lin, H. Zhang, B. Liu, Y. Wang, Y. Zhang, X. Sun, X. Cao, P. Hu, Q. Gao and Y. Tang, *Energy Environ. Sci.*, 2017, **10**, 1262–1271.
52 J. O. M. Bockris and E. C. Potter, *J. Electrochem. Soc.*, 1952, **99**, 169–186.